Composition Depth Profiles of Plasma-Fluorinated Poly(ethylene terephthalate) Fibers

JAMES A. McCAULLEY* and HARRIS A. GOLDBERG

Hoechst Celanese Research Division, 86 Morris Avenue, Summit, New Jersey 07901

SYNOPSIS

Composition depth profiles of the outer 50 Å of plasma-fluorinated poly(ethylene terephthalate) fibers were obtained by angle-dependent X-ray photoelectron spectroscopy (XPS). The effect of sample geometry on XPS sampling depth and the depth distribution function (DDF) was determined theoretically for cylindrical and hemispherical surfaces. The theoretical DDFs are nonexponential. For cylindrical surfaces, the effect is small, a 22% increase in surface sensitivity. The average XPS sampling depth for smooth, properly oriented fibers is shown to vary, as it does for a planar surface, as the sine of the nominal takeoff angle. The DDF appropriate for cylindrical surfaces was incorporated into a computer program for inversion of angle-dependent XPS data to obtain composition depth profiles of the fibers. Plasma-fluorinated PET fibers were used to demonstrate the use of angle-dependent XPS on fibers. XPS results indicate that most fluorination occurs within the top few "monolayers," attack is preferentially at the phenyl ring, both —CHF— and $-CF_2-$ moieties are formed, and fluorination causes partial loss of aromaticity. © 1994 John Wiley & Sons, Inc.

INTRODUCTION

X-ray photoelectron spectroscopy (XPS or ESCA) is by far the most widely used technique for analyzing polymeric surfaces. In an XPS experiment, the measured signal intensity from the ith core energy level of element j is given by an expression of the form

$$I_{ij}(\theta) = A\sigma_{ij} \int_0^\infty n_j(y')\,\phi_{ij}(y', \theta)\,dy' \qquad (1)$$

where y' is the depth; A, a constant containing various instrumental factors; σ_{ij}, the photoionization cross section; $n_j(y')$, the concentration depth profile of element j; and $\phi_{ij}(y', \theta)$, the depth distribution function (DDF) of signal from the ith core level of element j. The DDF describes the probability that a detected photoelectron originated at a depth y'. The takeoff angle, θ, is defined in Figure 1 as recommended by ASTM.[1] As this article concerns situations where the takeoff angle varies across a sample, we distinguish between the local takeoff angle, θ, and the nominal takeoff angle, θ_n, that is set experimentally. For a smooth, planar surface, $\theta = \theta_n$. Routine quantitative XPS analysis yields the "surface" atomic percentage of element j, N_j, as given by

$$N_j = \frac{(I_{ij}/S_{ij})}{\sum_j (I_{ij}/S_{ij})} \qquad (2)$$

where S_{ij} is an empirical sensitivity factor (the product of A and σ_{ij}) and the summation is performed over all elements detected.[2] This "surface" composition reflects the concentration depth profile averaged over a DDF to a typical depth of 50–100 Å. Neglecting elastic collisions, the DDF appropriate for a smooth, planar surface (using a detector accepting a narrow range of takeoff angles) is an exponential function (i.e., Beer–Lambert attenuation):

$$\phi_{ij}(y', \theta) = \frac{\exp(-y'/\lambda_{ij}\sin\theta)}{\lambda_{ij}\sin\theta} \qquad (3)$$

where λ_{ij} is the photoelectron attenuation length. The denominator normalizes $\phi_{ij}(y', \theta)$ at each θ.

* To whom correspondence should be addressed.

Journal of Applied Polymer Science, Vol. 53, 543–559 (1994)
 CCC 0021-8995/94/050543-17

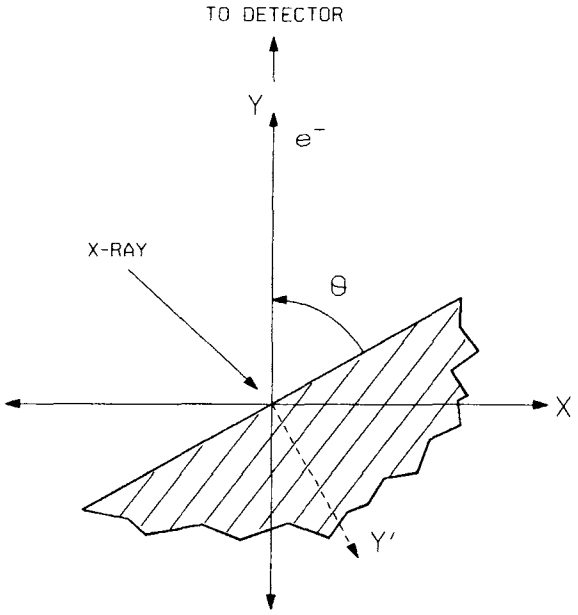

Figure 1 The XPS takeoff angle θ. The depth y' is defined as the distance along the surface normal Y' from which a detected photoelectron originates.

The surface sensitivity of XPS is usually expressed as a sampling depth or escape depth, D, which is defined as the depth normal to the surface at which the probability of a photoelectron escaping is $1/e$ (36.8%) times that at the surface.[1] Jablonski and Ebel concluded that in cases where the DDF is nonexponential it is misleading to use this definition of D. They described two experimental geometries (e.g., large acceptance angle detectors) where the DDF is nonexponential[3] and proposed that the definition of D be generalized to account for nonexponential DDFs. Noting that $\phi(y', \theta)$ is a probability distribution function,[4] Jablonski and Ebel proposed that D be defined as the mean value of the DDF:

$$D = \int_0^\infty y'\phi(y')\, dy' \qquad (4)$$

For a smooth, planar surface, this yields the expected result $D = \lambda \sin \theta_n$. Nonexponential DDFs can also be expected for samples (fibers, powders, etc.) that are not smooth and flat, because photoelectrons are accepted from a broad distribution of local takeoff angles. Gillberg and Kemp mentioned the difficulty, arising from the radial dependence of θ, of defining the XPS sampling depth for a cylindrical fiber.[5] The average escape depth of photoelectrons from these surfaces is less than from a smooth, planar surface, i.e., the surface sensitivity is increased.

If $\phi(y', \theta_n)$ is known, angle-dependent XPS data file. In an important contribution to the use of angle-dependent XPS, Tyler et al. described a computer program that employs a regularization algorithm to invert angle-dependent XPS data for smooth, flat surfaces with an assumed exponential DDF.[6] It should be noted that their program uses a slightly different DDF than that of eq. (3): Their kernel function is simply $\exp(-y'/\lambda \sin \theta)$, which is normalized only at $\theta = 90°$. It is of interest to extend the use of angle-dependent XPS to nonplanar surfaces such as polymeric fibers. For example, angle-dependent XPS might be useful for characterizing the surfaces of poly(ethylene terephthalate) (PET) tire cords that are treated to improve their adhesion in rubber.[7] Our wish to characterize the composition depth profiles at the surface of fibers motivated a study of the effect of sample geometry on angle-dependent XPS measurements. It is still widely believed that angle-dependent XPS is not applicable to nonplanar surfaces.[8] In this study, theoretical DDFs for fibers (cylindrical geometry) and random rough surfaces (modeled as a hemispherical surface) were determined. The DDF for a cylindrical surface was incorporated in the inversion program of Tyler et al.[6] This program was then used to obtain composition depth profiles from angle-dependent XPS measurements on plasma-fluorinated PET fibers. These experiments were performed not to validate the theoretical DDF for cylindrical fibers, but, rather, to demonstrate the technique on "real-world" fiber samples.

EXPERIMENTAL SECTION

Fiber Samples

Plasma-fluorination and XPS characterization were performed on 20 μm diameter (4 denier) melt-spun PET fibers in a 30 filament yarn (120 denier). About 1 m of yarn was wrapped around a flat Cu sample holder. The wrapped sample was then ultrasonically cleaned in three 25 mL aliquots of methanol for a total of 15 min. The sample was dried in a stream of high-purity N_2, mounted on the sample probe, and placed in the reaction chamber.

PET fibers were characterized by XPS at nominal takeoff angles $\theta_n = 15°$ and $\theta_n = 90°$ before plasma treatment to confirm surface cleanliness. Table I presents XPS results for clean PET fibers. At $\theta_n = 90°$, the observed composition is identical to that expected for PET; at $\theta_n = 15°$, a slight excess of carbon is observed. From results presented below,

Table I Surface Elemental Composition of Cleaned PET Fibers: Comparison of Experiment and Theory

θ_n	%C	%O
15°	72.9	27.1
	73.9	26.1
	71.7	28.3
	72.8 ± 1.1	27.2 ± 1.1
90°	71.1	28.9
	71.9	28.1
	70.2	29.8
	71.1 ± 0.8	28.9 ± 0.8
Theory	71.4	28.6

it is estimated that the escape depth, D, for a cylindrical fiber at $\theta_n = 15°$ is only ~ 6 Å, i.e., about one PET "monolayer." It is therefore possible that the excess carbon reflects the orientation of polymer chains at the surface, with phenyl groups at the surface screening ester linkages.

Remote Plasma Treatment

Plasma-fluorination of PET fibers was performed with a remote microwave plasma, using a discharge flow reactor[9] as a source of F atoms. The reaction chamber is connected to an XPS analysis chamber and is isolated during plasma treatment by closing a gate valve. Figure 2 is a schematic diagram of the reactor/analysis apparatus.

The flow tube is an alumina tube (0.94 cm i.d.) that enters the reaction chamber through an O-ring seal and ends ~ 1 cm from the sample surface. An air-cooled McCarroll microwave cavity (Opthos Instruments) is located ~ 70 cm upstream of the end of the flow tube. A right-angle Teflon fitting between the microwave cavity and the sample treatment point eliminated direct irradiation of the sample with vacuum ultraviolet (VUV) radiation from the plasma.

Ar (99.995%) carrier gas passed through a sorption purifier (MG Industries, Oxisorb HP). The carrier gas flow rate (100 sccm) was set with a stainless-steel metering valve and measured with an

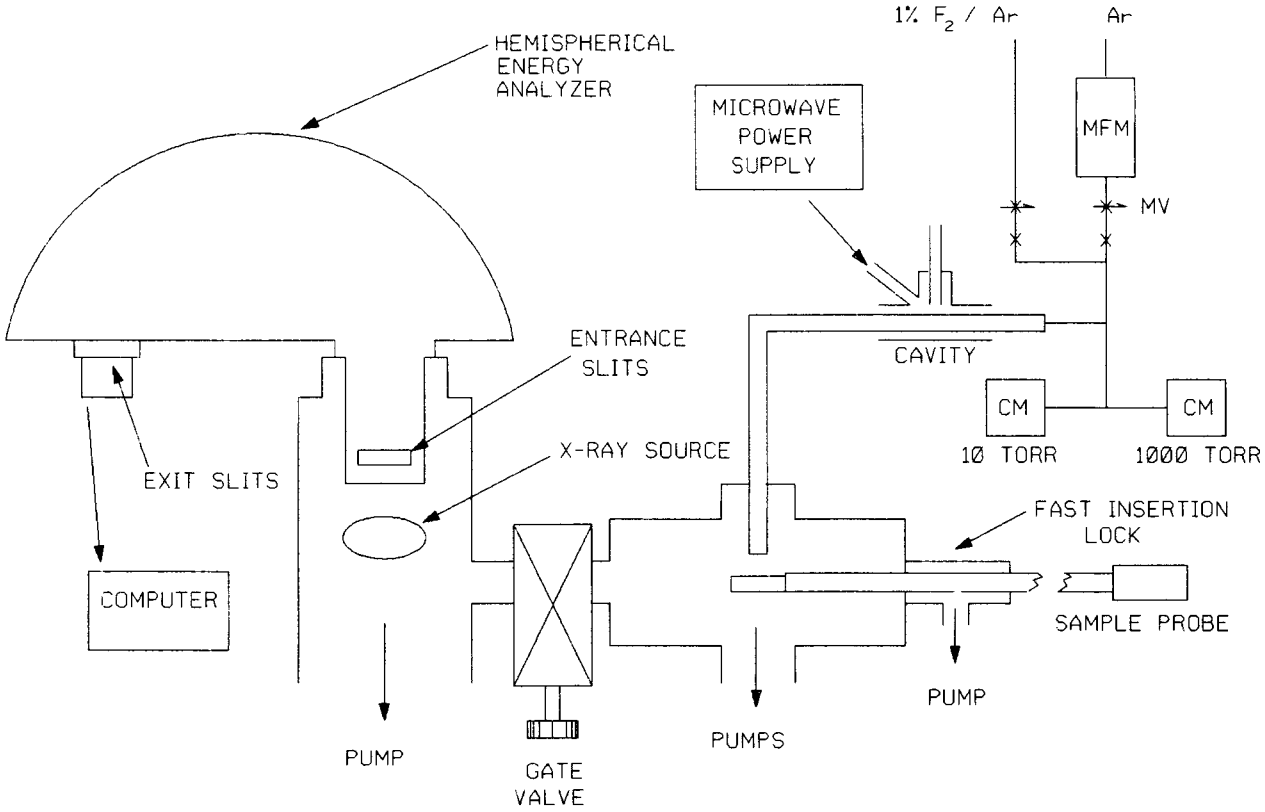

Figure 2 Schematic diagram of the apparatus: analysis chamber and plasma reactor. The abbreviations MFM, MV, and CM represent mass flow meter, metering valve, and capacitance manometer, respectively.

electronic mass flowmeter (Sierra, Model 821). The pressure was measured ~ 90 cm upstream of the microwave cavity with a capacitance manometer (MKS, Model 122, 10 or 1000 Torr). The viscous pressure drop between the point of measurement and the downstream end of the flow tube, calculated using Poiseuille's equation, is ~ 0.3 Torr, i.e., the actual pressure at the exit of the flow tube is ~ 6% lower than the measured pressure. The flow (~ 1 sccm) of the 1% F_2/Ar mixture was set with a stainless-steel metering valve; the flow rate was estimated from the incremental pressure rise in the reactor when the flow was turned on. The linear flow velocity in the flow tube was ~ 390 cm/s, yielding a transit time from the plasma to the sample of 180 ms. This is ample time for heterogeneous removal of ions and metastables produced in the plasma.

Fluorine atoms were generated in a microwave discharge of F_2 diluted (~ 0.01%) in Ar. The microwave power supply (2450 MHz, Opthos, Model MPG 4M) was operated at 50 W forward power. The plasma was initiated with a piezoelectric antistatic gun (Discwasher, Zerostat). It has been shown that F_2 dissociates with nearly unit efficiency under conditions similar to those used here.[10] Homogeneous recombination of F atoms is slow at this pressure[11] and can be discounted as a F atom loss process. First-order loss at the alumina flow tube wall, however, occurs at a rate of ~ 10 s^{-1},[11] indicating that the F atom concentration is reduced by about a factor of seven during the flow tube transit time. Given the known number density of F_2 in the flow tube ($[F_2] = 1.6 \times 10^{13}$ cm^{-3}), the assumed unit dissociation efficiency, and the approximate heteogeneous loss rate, we estimate the F atom concentration at the exit of the flow tube to be ~ 2×10^{12} cm^{-3}. We have not characterized the flow field between the end of the flow tube and the sample surface, but estimating a twofold divergence of the diameter of the "plume" at the end of the flow tube, this suggests a F atom concentration of ~ 5×10^{11} cm^{-3} (or partial pressure 10^{-5} Torr). This yields an isotropic flux at the fiber surface of ~ 10^{16} F atoms cm^{-2} s^{-1}. The maximum F atom dose (3×10^{17} F

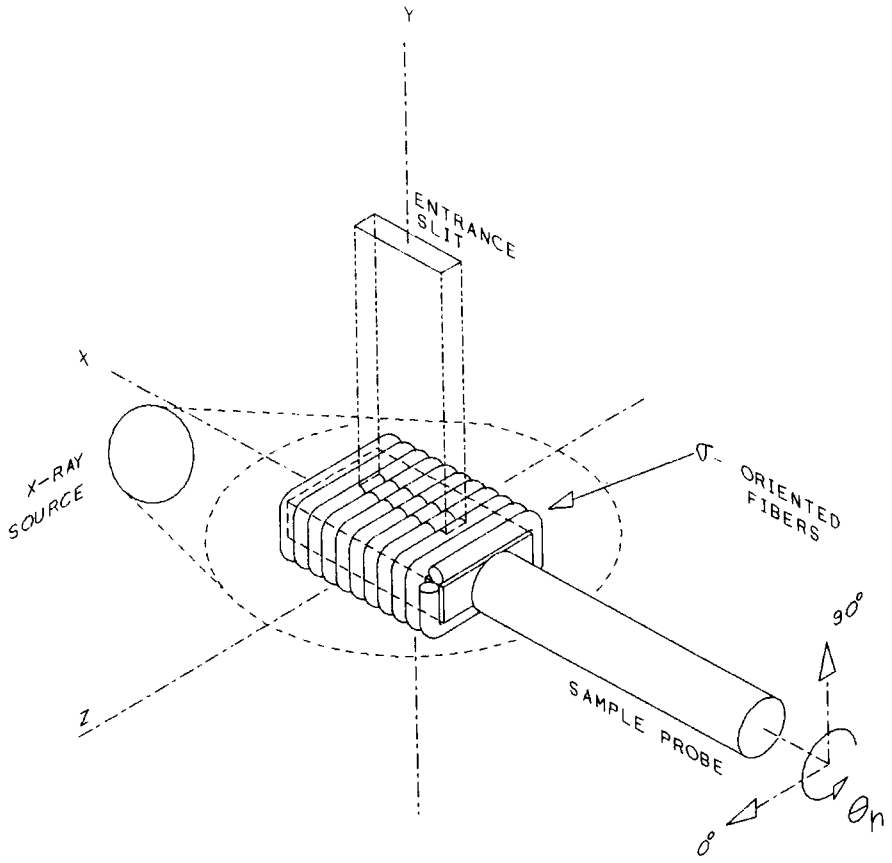

Figure 3 Schematic diagram (not to scale) of the orientation of a fiber relative to the entrance slit of the energy analyzer. The diameter of the fiber is greatly exaggerated for clarity.

atoms cm^{-2} in 30 s) on these fiber samples was insufficient to cause roughening (i.e., by etching) on a length scale that would preclude angle-dependent XPS measurements.

XPS Analysis

XPS experiments were performed with a Kratos ES300 X-ray photoelectron spectrometer. The base pressure is $\sim 1 \times 10^{-10}$ Torr, but the pressure increased to $\sim 2 \times 10^{-8}$ Torr when the isolation gate valve was opened to analyze the fiber samples. A nonmonochromatic AlKα X-ray flood source irradiated the sample. The X-ray source was operated at low power (12 kV and 10 mA emission current) to minimize sample damage. The hemispherical energy analyzer was operated with a fixed retardation ratio of 23 : 1. To minimize X-ray-induced loss of fluorine, the data collection time was reduced by using the widest analyzer slits (5 mm).

A copper probe tip was attached to a heatable/coolable stainless-steel probe that entered the analysis chamber through a differentially pumped load lock with spring-loaded Teflon seals. Variation of the nominal takeoff angle, θ_n, was achieved by rotating the probe shaft around its axis; it was fitted with a ruled collar for setting the takeoff angle. Initial angular alignment of the sample was done visually with an estimated accuracy of ±3°. The entrance slit of the energy analyzer was 5 × 22 mm, with the long axis parallel to the sample rotation axis (see Fig. 3). The slit was ~ 85 mm above the sample, yielding a collection angle of ~ 3° along the short axis and ~ 15° along the long axis. According to Tyler et al., such a slit geometry is a good choice for angle-dependent XPS, as a compromise between angular resolution and sensitivity.[12]

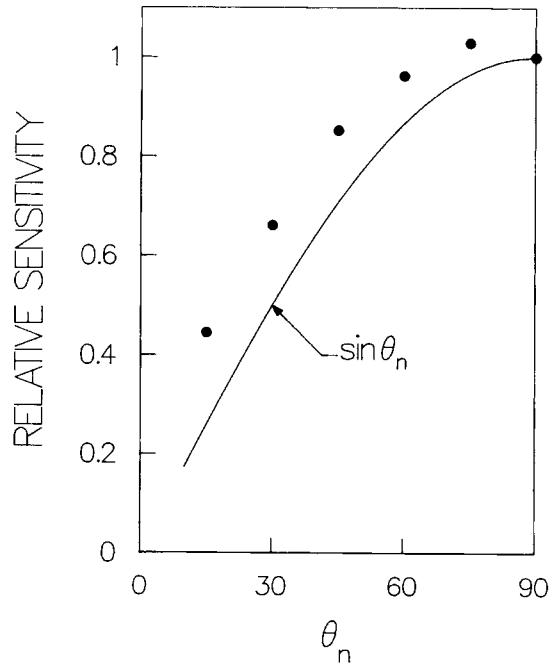

Figure 4 Relative sensitivity of the Kratos ES300 as a function of the nominal takeoff angle. Also shown is $\sin\theta_n$.

Table II Angle-dependent Sensitivity Factors Measured for the Kratos ES300

θ_n	Factor
90°	1.000
75°	0.939
60°	0.900
45°	0.830
30°	0.756
15°	0.581

After fluorination, core level spectra were acquired for C1s (~ 3 min), O1s (~ 3 min), and F1s (~ 3 min) levels at θ_n = 15°, 30°, 45°, 60°, 75°, and 90°. The sequence was chosen at random to minimize systematic error due to X-ray-induced sample damage. Total data acquisition time for angle-dependent XPS measurements on a sample was ~ 1 h.

Data Analysis

This data analysis procedure comprises three steps: measurement of core level peak intensities for a set of takeoff angles, normalization of peak intensities, and inversion of normalized XPS data with the regularization program of Tyler et al.[6]

The integrated intensities of core level peaks were measured after "Shirley" background subtraction.[13] Two normalization steps, one angle-independent and the other angle-dependent, followed. The former is accomplished by dividing the raw peak intensities by empirical sensitivity factors, S_{ij}: 1.00 for C1s, 1.70 for O1s, and 2.27 for F1s. These factors, which were measured in earlier experiments on clean PET and polytetrafluoroethylene films at θ_n = 90°, normalize the measured intensity with respect to photoionization cross section, analyzer transmission function, and kinetic energy dependence of the photoelectron attenuation length.

The sensitivity of the Kratos ES300 is a function of θ_n, decreasing sharply below ~ 60°. Instrumental factors that vary with angle, thereby contributing to this effect, include X-ray flux, field of view of the energy analyzer, and overlap of the irradiated area

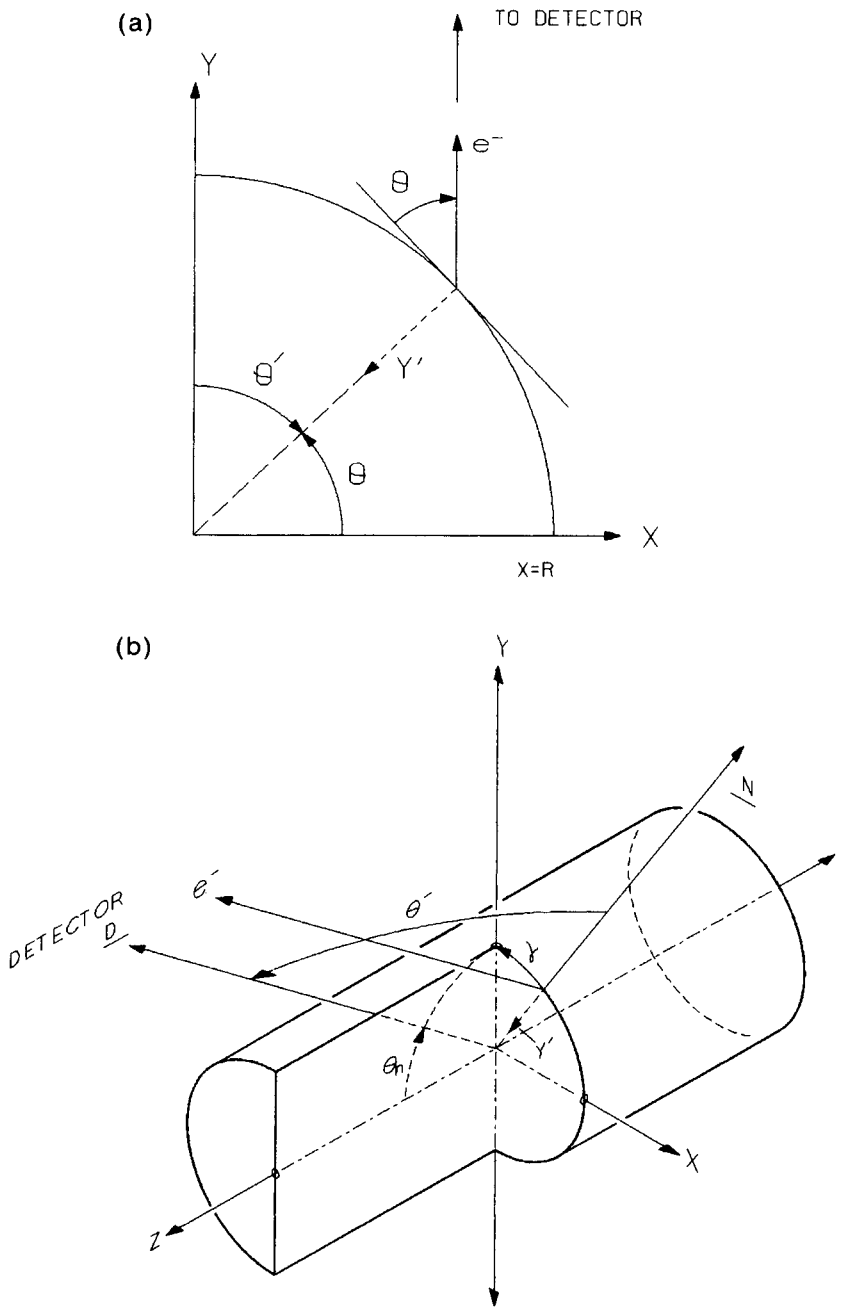

Figure 5 Geometry of XPS analysis of cylindrical surfaces at (a) $\theta_n = 90°$ and (b) as a function of θ_n. (c) Geometry of analysis of a hemispherical surface.

and the field of view of the energy analyzer. The inversion program of Tyler et al. anticipates that the integrated intensity of any core level peak from a homogeneous sample (e.g., clean Au) will vary as sin θ_n. Tyler suggested the use of data from a clean Au surface to obtain correction factors for angle-dependent normalization of data from nonuniform samples.[14] Figure 4 shows the angle-dependent sensitivity of the Kratos ES300, measured using a sputter-cleaned Au film (1000 Å) on a Si wafer. Also shown in Figure 4 is the sin θ_n dependence expected by the inversion program. Table II presents the multiplicative factors needed to make the angle-dependent Au data comply with a sin θ_n dependence; these factors were used to normalize the integrated intensities of the core level peaks from the plasma-

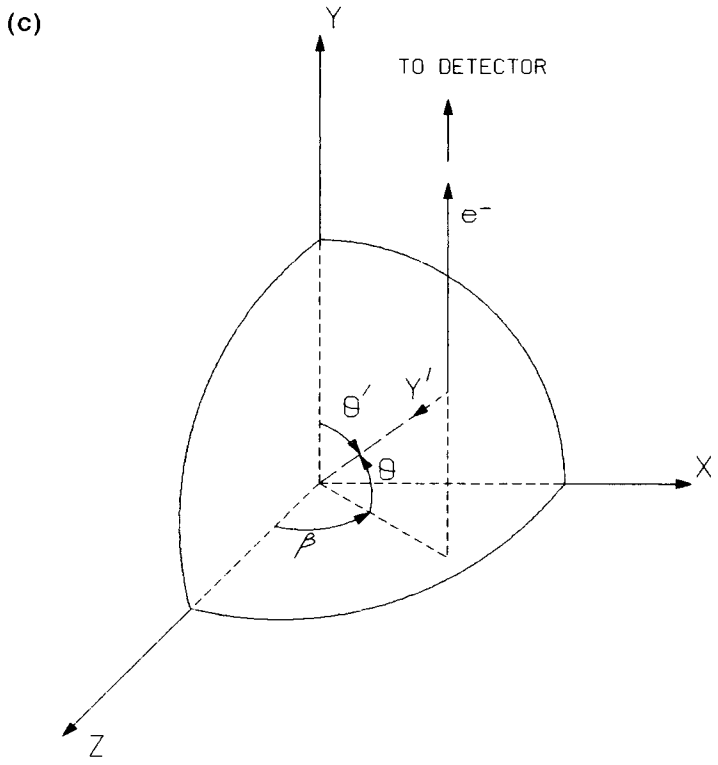

Figure 5 *(Continued from the previous page)*

fluorinated PET films. The sum of normalized peak intensities at each angle varies approximately as $\sin \theta_n$.

The only other data required as input for the inversion program are photoelectron attenuation lengths. The values used here (C1s, 35 Å; O1s, 30 Å; F1s, 27 Å) were obtained from an expression [λ (Å) = $0.022E_K + 9.0$; E_K = photoelectron kinetic energy] reported by Laibnis et al.[15] Although this expression was obtained for alkanethiol self-assembled monolayers on Au, the values it yields are probably as reliable for other organic surfaces (e.g., PET) as those available from any other source. These values are ~ 6% greater than those used by Tyler et al., who used the expressions of Seah and Dench.[16]

The regularization algorithm employs a smoothing parameter (or regularizing operator[17]), α, which is varied in the inversion program of Tyler et al. to minimize the mean-squared deviation (or error) between measured core level peak intensities and those regenerated from a trial composition depth profile. Tyler et al. also discussed other strategies for determining the optimum value of α.[6] Error "surfaces," plots of the error vs. α, were generated during inversion of angle-dependent XPS data from plasma-fluorinated PET fibers. Because selection of α is important, these are discussed below.

Determination of the DDF appropriate for cylindrically symmetric fibers is described below. The resulting DDF was expressed as an empirical function and incorporated in the inversion program of Tyler et al.

THEORY

In the Kratos ES300, a fiber may be oriented with its axis parallel to the plane defined by the X-ray source, the detector, and their mutual projection on the fiber surface (the yz-plane in Fig. 3). Here, this will be called a σ-oriented fiber. Conversely, the axis of a π-oriented fiber is perpendicular to the plane defined by the X-ray source, the detector, and their projection on the fiber surface. Varying θ_n for a π-oriented fiber will have no effect except for shadowing at small θ_n. In the Kratos ES300, it is convenient to prepare a "raft" of parallel, σ-oriented fibers for angle-dependent XPS (see Fig. 3).

It is assumed that photoelectrons travel a straight-line path through a sample, parallel to the y-axis (along which the detector is located if $\theta_n = 90°$), i.e., elastic scattering and the finite acceptance angle of the detector are neglected. Beer–Lambert attenuation of the photoelectron flux (in the sample)

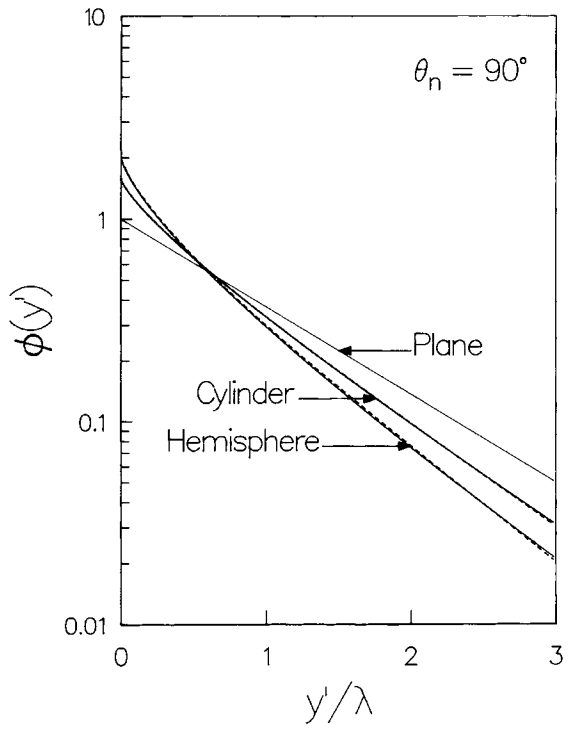

Figure 6 Theoretical DDFs for planar, cylindrical, and hemispherical surfaces at $\theta_n = 90°$. The solid lines for the cylindrical and hemispherical DDFs were obtained by numerical integration of eqs. (5) and (12). The dashed lines are triple-exponential fits to the DDFs.

along the y-axis is assumed. Because the $1/e$ attenuation length of X-rays ($\sim$ 8.2 and $\sim$ 5.1 μm for AlKα and MgKα X-rays impinging on PET) is much greater than that of photoelectrons in a solid, attenuation of the incident X-ray beam in the fiber is neglected. Photoelectrons produced below the midplane of the fiber are neglected because they are unlikely to enter the detector without significant energy loss.

Cylindrical Surfaces at $\theta_n = 90°$

A cylindrical surface [see Fig. 5(a)] can be viewed as an infinite series of planar area elements having takeoff angles ranging from 0° (at $x = R$, the fiber's radius) to 90° (at $x = 0$). Thus, for a cylindrical surface at $\theta_n = 90°$, one obtains the normalized DDF by integration over θ:

$$\phi(y') = \int_0^{\pi/2} \exp(-y'/\lambda \sin\theta)\, d\theta \qquad (5)$$

Figure 6 presents the DDF (solid line) of a cylindrical surface (at $\theta_n = 90°$) obtained by numerical integration of eq. (5). Also presented in Figure 6 is a triple-exponential fit (dashed line) to the DDF. The coefficients (A_i and a_i) of the triple-exponential function,

$$\phi(y') = A_1\exp(-y'/a_1\lambda) + A_2\exp(-y'/a_2\lambda) + A_3\exp(-y'/a_3\lambda) \qquad (6)$$

are presented in Table III. The average escape depth, D, at $\theta_n = 90°$ is 0.778λ, $\sim$ 22% smaller than that of a smooth, planar surface. This DDF is also appropriate for π-oriented fibers at $\theta_n = 90°$. The $\sim$ 15° collection angle in the xy-plane is small enough (see Ref. 3) that it should have little effect on the DDF of π-oriented cylindrical fibers.

Angle-dependent XPS on Cylindrical Surfaces

The physical basis of the angle-dependent XPS method is that the escape depth from a smooth, planar surface varies as sin θ. Therefore, sin θ appears as a length-scale factor in the denominator of the exponential function's argument [see eq. (3)]. Here it shown that the escape depth from a σ-oriented fiber varies as sin θ_n as depicted in Figure 5(b). Rather than rotating the fiber about the x-axis, consider the equivalent scheme of rotating the detector to an angle θ_n in the yz-plane as shown in Figure 5(b).

The angle between a vector (**N**) normal to the surface of a fiber and a vector (**D**) from the origin to the detector is the complement of the local takeoff angle θ. This angle, θ', can be determined using the scalar product of two unit vectors pointing in these

Table III Coefficients of a Triple Exponential Representation: $\phi(y') = A_1\exp(-y'/a_1\lambda) + A_2\exp(-y'/a_2\lambda) + A_3\exp(-y'/a_3\lambda)$ of the Depth Distribution Functions (at $\theta_n = 90°$) for Cylindrical and Hemispherical Surfaces

Surface	A_1	a_1	A_2	a_2	A_3	a_3
Cylinder	0.4359	0.3096	0.1244	0.05902	0.9987	0.8565
Hemisphere	0.7214	0.2753	0.2237	0.05348	1.031	0.7616

directions. The unit vector pointing toward the detector is

$$\mathbf{D} = \cos\theta_n \mathbf{z} + \sin\theta_n \mathbf{y} \quad (7)$$

[see Fig. 5(b)]. The unit vector normal to the surface of the fiber is

$$\mathbf{N} = \cos\gamma \mathbf{y} + \sin\gamma \mathbf{x} \quad (8)$$

The complement, θ', of the local takeoff angle, θ, is thus given by

$$\cos\theta' = \cos\gamma \sin\theta_n \quad (9)$$

and

$$\sin\theta = \cos\gamma \sin\theta_n \quad (10)$$

By substituting this in eq. (5), one obtains the DDF that explicitly includes the nominal takeoff angle:

$$\phi(y', \theta_n) = \int_0^{\pi/2} \exp(-y'/\lambda \cos\gamma \sin\theta_n)\, d\gamma \quad (11)$$

where γ is the complement of θ in eq. (5). In keeping with the computer program of Tyler et al., the DDF used for analysis of data acquired from fibers was normalized only at $\theta_n = 90°$.

Hemispherical Surfaces

For a randomly rough surface that is nominally flat, all possible takeoff angles are equally likely and azimuthal symmetry (on average) obtains, a situation equivalent to analysis of a smooth hemispherical surface. In the absence of shadowing effects (which should contribute at small θ_n), the sampling depth is independent of θ_n.

For a hemispherical surface [see Fig. 5(c)],

$$\phi(y') = \int_0^{\pi/2} \exp(-y'/\lambda \cos\theta')\sin\theta'\, d\theta' \quad (12)$$

where $\sin\theta'\, d\theta'$ is the differential element for integration over θ' in spherical coordinates. Integration over the azimuthal angle, β, is obviated by normalization. An analytical solution to a generalized version of this equation was presented by Jablonski and Ebel in a discussion of DDFs appropriate to instruments having various acceptance angles.[3] They apparently did not appreciate that this DDF might also be appropriate for analysis of a rough surface with a detector having a narrow acceptance angle. Figure 6 presents the DDF of a hemispherical surface obtained by numerical integration and normalization of eq. (12). This DDF is identical to that reported by Jablonski and Ebel for a detector collecting 2π Sr.[3] Also presented in Figure 6 is a triple-exponential fit to the hemispherical DDF. The coefficients (A_i and a_i) of the triple-exponential function are presented in Table III. The escape depth, D, at $\theta_n = 90°$ is 0.667λ, a third smaller than that of a smooth, planar surface. Although this DDF is independent of θ_n, and therefore not useful for angle-dependent XPS measurements, it is needed to correctly interpret XPS data from rough surfaces. It should also prove useful for separating effects of sample geometry and sample roughness in angle-dependent XPS measurements on samples having partially roughened surfaces.

RESULTS AND DISCUSSION

Angle-dependent XPS Results

Figure 7 compares an XPS survey spectrum of clean PET fiber to that of PET fiber fluorinated for 15 s.

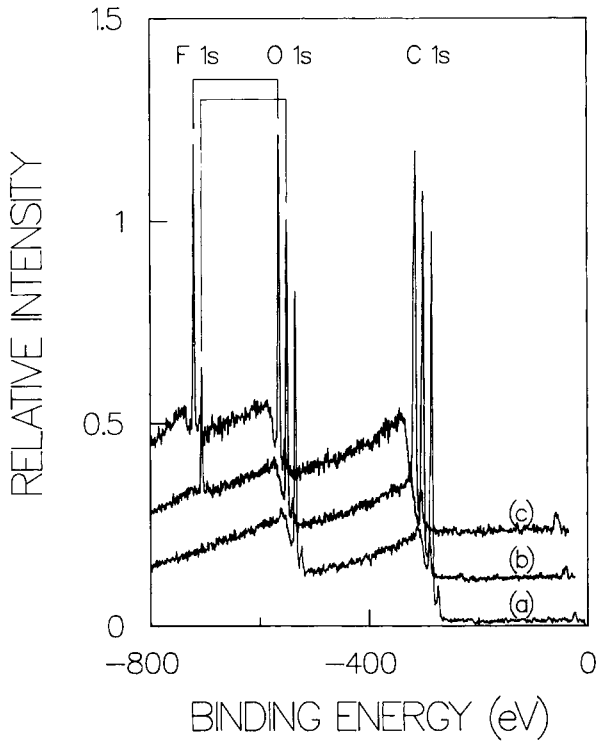

Figure 7 XPS survey spectra of PET fiber (a) before fluorination, (b) after 15 s fluorination ($\theta_n = 90°$), and (c) after 15 s fluorination ($\theta_n = 15°$). Spectra (b) and (c) have been shifted vertically and horizontally to prevent overlapping of peaks.

Because the spectrum of clean PET is nearly identical at $\theta_n = 90°$ and $\theta_n = 15°$ (see Table I), only one spectrum is shown. In contrast, there is a large difference between spectra of plasma-fluorinated PET at these angles. Note the increased F/O ratio at $\theta_n = 15°$. This simple qualitative result reveals two facts: the F concentration varies over the XPS sampling depth and the variation of sampling depth with θ_n required for inversion of angle-dependent XPS data is retained by this fiber sample, i.e., the fiber surface is sufficiently smooth. To obtain a composition depth profile, one must simply invert the data using the correct DDF.

Table IV presents normalized, angle-dependent peak intensities of PET fibers fluorinated for 2, 15, and 30 s. These data were inverted using the regularization program of Tyler et al. in three variations: using the exponential DDF of a planar surface, using the nonexponential DDF of a cylindrical surface, and using an exponential DDF incorporating reduced λ values ($0.778\lambda_{ij}$) that simulate the decreased sampling depth from a cylindrical surface. This is analogous to approximating the nonexponential DDF from elastic scattering with an exponential DDF incorporating experimental attenuation lengths.

Figure 8 shows how a composition depth profile depends on the smoothing parameter, α. The "sharpness" (i.e., $d[F]/dy'$ near $y' = 0$ in Fig. 8) increases dramatically with decreasing α. Proper choice of α is therefore an important consideration. The inversion program of Tyler et al. varies α to minimize the fitting error (the sum-of-squared de-

Table IV Fully Normalized Angle-dependent XPS Core-level Peak Intensities of Plasma-fluorinated PET Fibers

Duration	θ_n	C1s	O1s	F1s
2 s	15°	5716	1975	294
	30°	12835	4585	536
	45°	16602	5855	518
	60°	19846	7187	498
	75°	20698	7972	575
	90°	20760	8083	732
15 s	15°	5267	2051	1031
	30°	11162	4420	1889
	45°	13880	5610	2022
	60°	15655	6188	1929
	75°	16432	6606	1882
	90°	16080	6502	1924
30 s	15°	5675	2524	797
	30°	12099	4935	1374
	45°	15602	6310	1431
	60°	19116	7834	1585
	75°	19379	8260	1590
	90°	19411	8281	1646

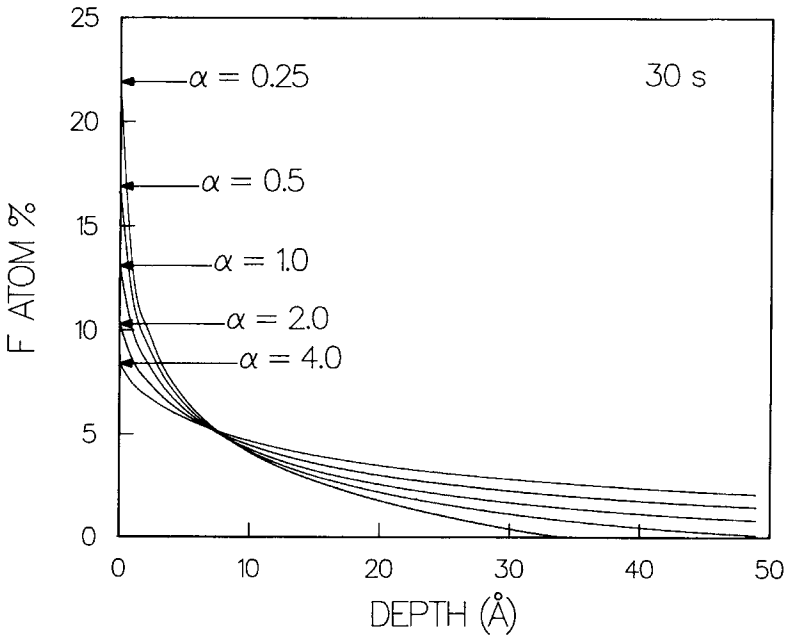

Figure 8 Comparison of F atom % depth profiles of a plasma-fluorinated PET fiber (30 s) obtained using values of the smoothing parameter, α, ranging from 0.25 to 4.0. The curves cross at ~ 7 Å, with the order (from top to bottom) inverted beyond the crossing.

viations between measured and calculated intensities). Figure 9(a)–(c) presents one-dimensional "error surfaces" for inversion of angle-dependent XPS data from fluorinated PET fibers, with α treated as a fitting parameter. These curves show how the inversion error depends on α. The solid lines are results for inversion using an exponential DDF (assumed planar surface); the dotted lines result from using the DDF for a cylindrical surface. Note the similarity of the surfaces for different treatment durations. In all three cases, the error is smaller when using the exponential DDF than that appropriate for a cylindrical surface. This may be a result of the increased surface sensitivity of the latter DDF; it obviously cannot be taken as evidence that the fibers are planar. Because of severe smoothing, all the error surfaces are relatively flat for $\alpha > 2$. At $\alpha < 0.25$, the inversions were unstable and resulting composition depth profiles deviated wildly from that of pure PET at depths > 50 Å. Our criterion for selecting α was to choose the minimum value that yielded a stable result and a "reasonable" composition below ~ 50 Å. This, of course, assumes prior knowledge of the bulk composition of the sample. The α values used were 0.5, 1.0, and 0.5 for the 2, 15, and 30 s treatments.

The resulting composition depth profiles are presented in Figure 10(a)–(c). Note that in all cases the F concentration decreases by more than half within ~ 10 Å of the surface. This distance is approximately twice the average (a-axis and b-axis) diameter of a PET chain; most of the fluorination occurs within the top few "monolayers" of PET. At a depth of 50 Å, the compositions of plasma-fluorinated fibers agree reasonably well [especially in Fig. 10(a) and (c)] with that of pure PET.

To evaluate the importance of using the nonexponential DDF when analyzing fibers, a direct comparison of the results obtained using the DDFs appropriate for planar and cylindrical surfaces was done. A fair comparison requires that the same value of α be used. Figure 11 compares the F depth profiles for plasma-fluorinated PET fiber obtained using the DDFs appropriate for planar and cylindrical surface geometries. The two DDFs yield the same elemental composition at $y' = 0$. As expected, the F depth profile is steeper, and the integrated F concentration is ~ 22% less, when the cylindrical DDF is used. Given the uncertainty from other sources (e.g., selection of α), the agreement between these results may be good enough that the exponential DDF is satisfactory for most analyses. One can get somewhat better results with an exponential DDF by using attenuation lengths that have been reduced to reflect the decreased sampling depth in a fiber. Figure 11 contains the F profile obtained using reduced attenuation lengths ($0.778\lambda_{ij}$) in the exponential DDF. The profile agrees reasonably well with that obtained using the nonexponential DDF. Accurate quantitative results require use of the correct DDF.

Implications for Fiber Surface Analysis

Although these results were obtained on melt-spun PET fibers having a circular cross section, this should not be construed as a restriction on the use of angle-dependent XPS to cylindrical melt-spun fibers. Analysis of smooth fibers having other cross-sectional shapes (e.g., trilobal) should be possible. If a sufficient number of fibers are randomly oriented around their axes, cylindrical symmetry is, on average, retained.

Sources of error in these composition depth profiles include attenuation lengths, XPS peak intensities, angle measurements, sensitivity factors, measured normalization factors, selection of α, and deficiencies of the model. Laibnis et al. reported a total uncertainty of ~ 15% for their attenuation length values.[15] Random errors in measured XPS peak intensities should be negligible (< 5%); systematic errors (e.g., from X-ray-induced sample damage) can be minimized by experimental procedures. Sensitivity factors and normalization factors can be measured with better than 5% uncertainty.

As discussed above, the composition depth profile is very sensitive to the value of α. Here, a minimal smoothing approach, choosing the smallest α that yields a stable depth profile, was used. Minimizing the difference between measured intensities and regenerated intensities, as done in the inversion program of Tyler et al., may be preferable, but the uncertainties of the measured intensities should be included. This has been emphasized by Smith and Livesey, who also note the desirability of using prior information if available.[18] At some level, further decreases in the variance become statistically meaningless; a χ^2 statistic is needed. In any event, a minimal smoothing criterion may be necessary if the χ^2 surface is too flat.

This model could be improved by inclusion of elastic scattering in the DDFs. This should be relatively easy as this topic has lately received much attention. Werner and Stori presented a simple empirical expression that accounts for the effect of elastic scattering on the DDF.[19] This could be incorporated in the inversion program of Tyler et al. Inclusion of elastic scattering should, however, have little effect on the results presented here because

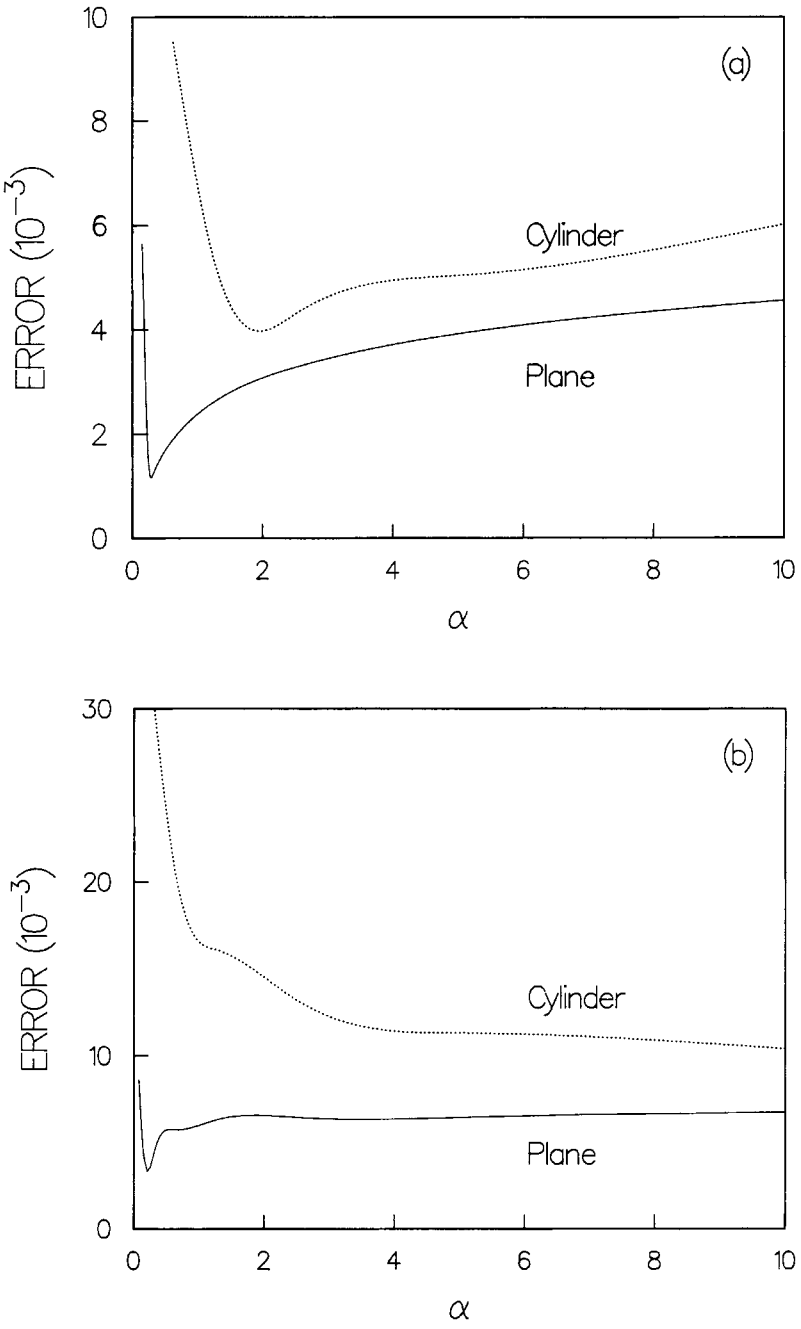

Figure 9 Error surfaces for inversion of angle-dependent XPS data from PET fibers treated for (a) 2 s, (b) 15 s, and (c) 30 s. For each treatment time, the error surfaces resulting from use of DDFs appropriate for planar and cylindrical surfaces are presented.

the fluorinated layers are very thin and experimental attenuation length values (which intrinsically include elastic scattering) were used.

Thus, there is still room for improvement: experimental procedures, inclusion of elastic scattering, selection of the regularizing operator, quantifying error sources by study of model systems, and characterizing the effect of surface roughness. The performance of the entire angle-dependent XPS analysis "system" (experimental procedures and data analysis) can be assessed by analysis of surface layers with well-characterized structures. Toward

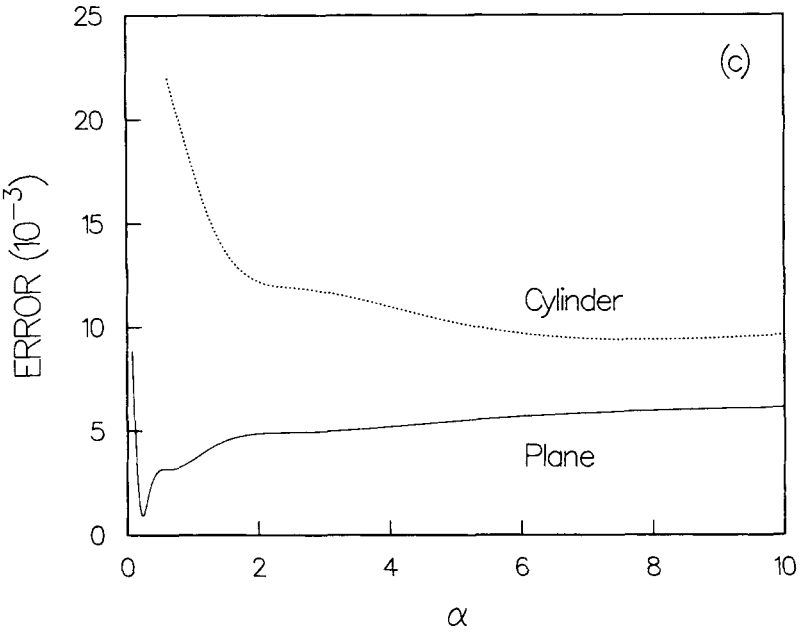

Figure 9 *(Continued from the previous page)*

this end, we have been performing angle-dependent XPS measurements on self-assembled alkanethiol monolayers on Au surfaces.[20] The effects of surface roughness and geometry are being studied.

Fluorination Mechanism

Table V presents the surface compositions [obtained using eq. (2)] of fluorinated PET fibers at $\theta_n = 15°$ and $\theta_n = 90°$. The F concentration is higher on the sample treated for 15 s than the one treated for 30 s; the difference is outside the XPS measurement uncertainty. The discrepancy reflects the irreproducibility of the plasma treatments. With better control of the F_2 flow, this could be improved. These results suggest that the surface concentration of fluorine saturates after ~ 15 s. Based on the estimated F-atom flux presented above, this corresponds to a F-atom exposure of ~ 10^{17} F atoms/cm^2. Saturation of the surface fluorine concentration during plasma fluorination of organic surfaces has been reported previously.[21-23] In their recent study of fluorination of alkanethiol self-assembled monolayers (SAMs) on Au surfaces, Robinson et al.[21] observed an approach to saturated fluorine uptake at ~ 10^{17} F atoms/cm^2, consistent with the present finding for fluorination of PET. Strobel et al. attributed saturation of fluorine concentration on polymeric surfaces to a competition between fluorination and etching.[22,23] Robinson et al. concluded that saturation during fluorination of self-assembled monolayers was caused by steric blocking that prevented further inward diffusion of F atoms.

The composition depth profiles presented in Figure 10 graphically depict the penetration depth of plasma fluorination. Strobel et al. used angle-dependent XPS to estimate the depth (50–100 Å) of fluorination of polyolefins and polystyrene, but did not invert the data to obtain depth profiles. Robinson et al. estimated that the top six carbon atom layers in SAMs were fluorinated. This corresponds to a depth of ~ 8 Å, reasonably consistent with the present results. As the accuracy of angle-dependent XPS depth profiling is refined, it should become a valuable tool for investigating the mechanisms of plasma surface modifications.

Table V Surface Elemental Composition of Plasma-fluorinated PET Fibers

Duration	θ_n	%C	%O	%F
2 s	15°	71.6	24.7	3.7
	90°	70.2	27.3	2.5
15 s	15°	63.1	24.6	12.3
	90°	67.8	25.6	6.6
30 s	15°	63.1	28.0	8.9
	90°	66.2	28.2	5.6

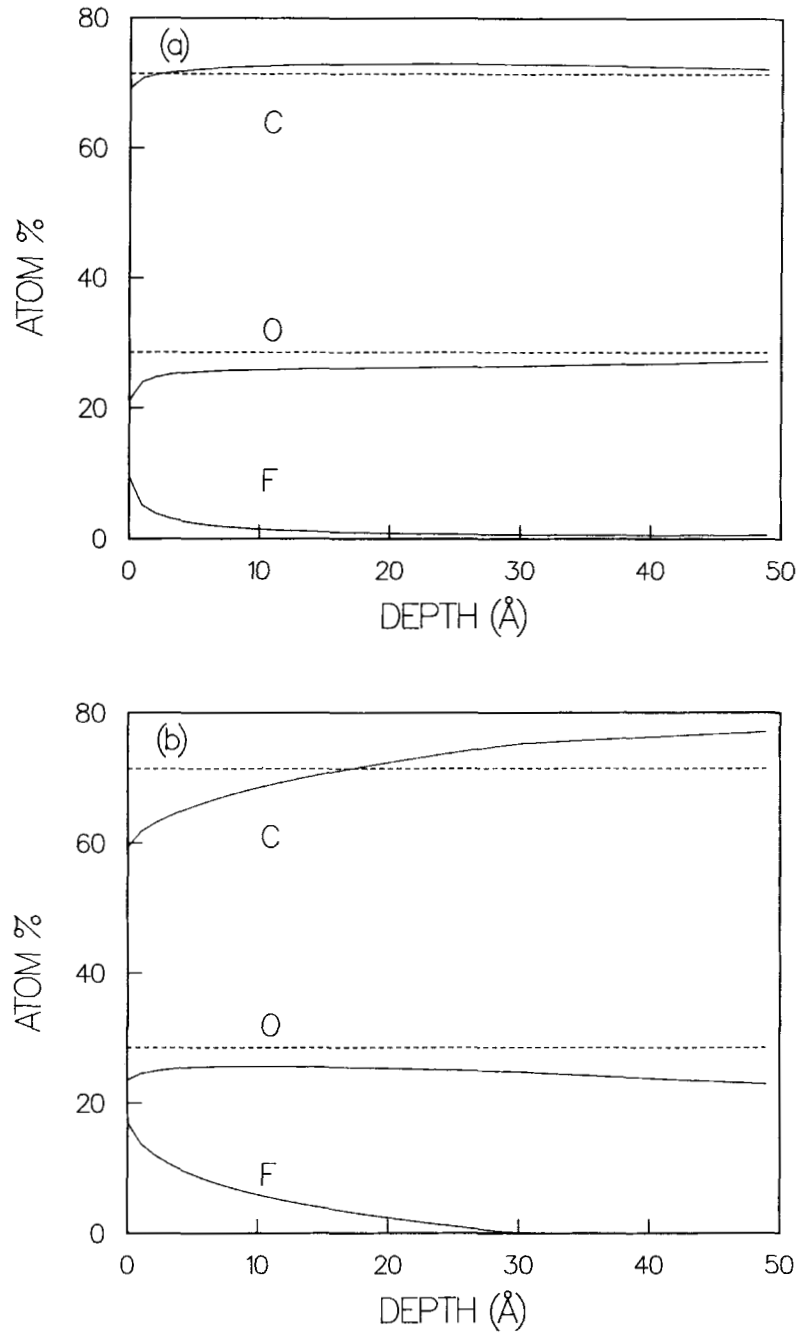

Figure 10 Composition depth profiles for plasma-fluorinated PET fibers treated for (a) 2 s, (b) 15 s, and (c) 30 s. The α values used were 0.5, 1.0, and 0.5, respectively. The dashed lines represent the C and O atom percentages in pure PET.

Figure 12 presents C1s spectra at $\theta_n = 15°$ before and after 15 s plasma fluorination. The total C1s intensity decreased by ~ 7%, apparently a result of screening by F grafted to the surface. Also presented in Figure 12 is the C1s difference spectrum (fluorinated − unfluorinated), revealing loss of intensity on the low binding energy side of the main peak and appearance of two new features at higher binding energy. The "loss feature" is at ~ 284.5 eV, typical of C—C, H moieties. This indicates that fluorination preferentially occurs on the phenyl rings in PET, not on the —CH_2CH_2— linkages, which have

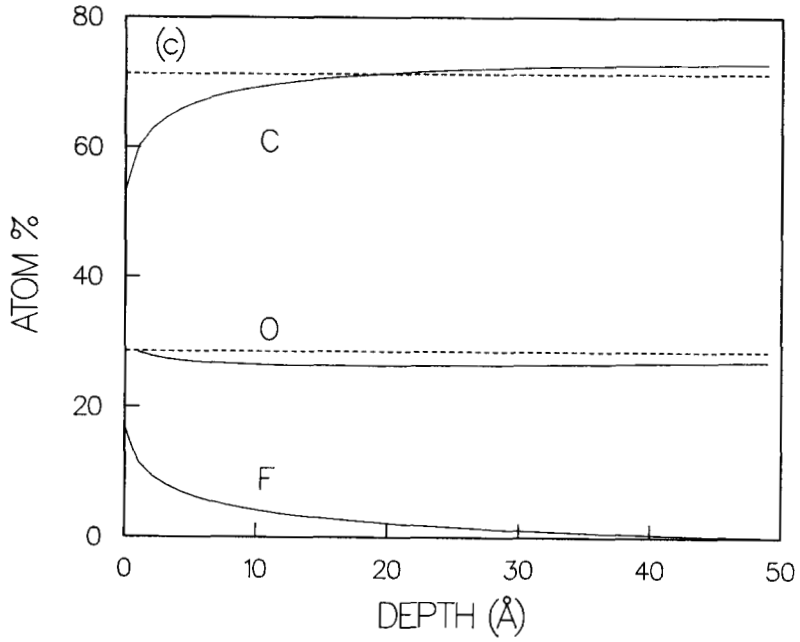

Figure 10 *(Continued from the previous page)*

their C1s binding energy chemically shifted to ~ 286 eV (because these C atoms are bonded to O atoms). Preferential attack at π-clouds of phenyl rings, by formation of free radical adducts, is well documented in reactions of other free radicals (e.g., hydroxyl) with aromatic molecules in the gas phase.[24] The two new features have binding energy shifts, ΔE_b, 3.2 and 5.5 eV relative to the C—C,H "loss

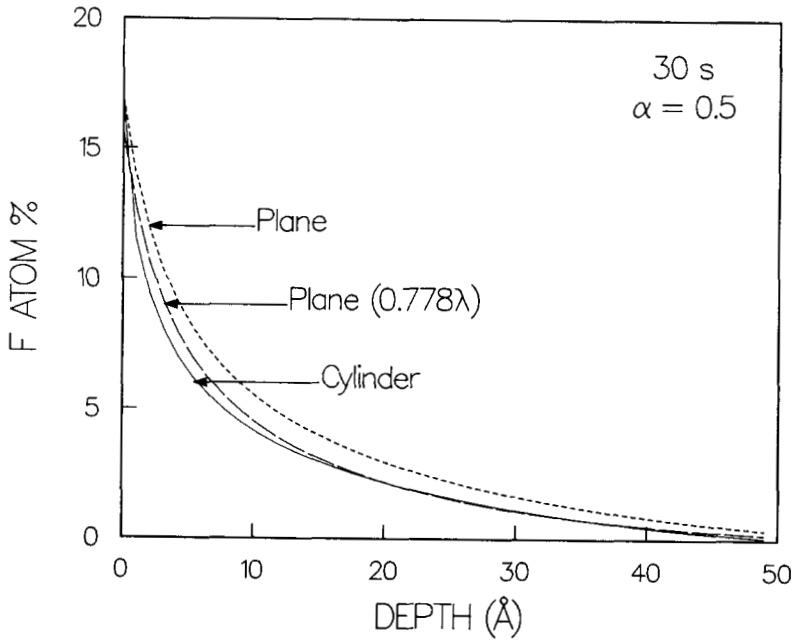

Figure 11 Comparison of F atom % depth profiles for plasma-fluorinated PET fiber obtained using the DDFs appropriate for planar and cylindrical surface geometries. Also shown is the profile obtained by using a reduced attenuation length (0.778 λ) in the exponential DDF.

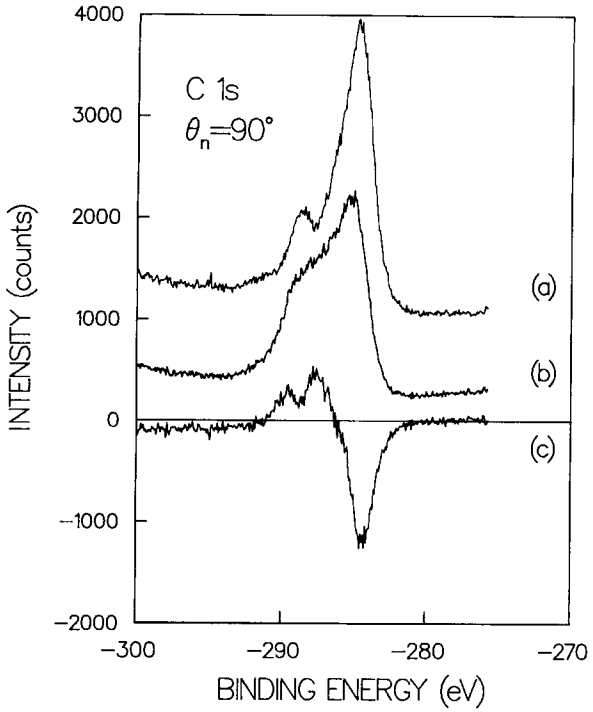

Figure 12 C1s spectra of PET fiber (a) before and (b) after 15 s plasma fluorination. Also shown is (c) the difference spectrum (b − a) that reveals loss of C—C, H and formation of —CHF— and —CF_2— moieties. Spectrum (a) has been shifted upward by 1000 counts for clarity.

feature." These energies correspond reasonably well with those reported for —CHF— and —CF_2— moieties, ca. 2.9 eV per F atom substituent.[25] Robinson et al. found formation of —CHF— and —CF_2— moieties in F-atom fluorination of self-assembled monolayers of alkanthiols on Au.[21] Formation of —CF_2— groups during attack at the phenyl rings in PET implies partial loss of aromaticity. Strobel et al. observed loss of aromaticity in SF_6 plasma fluorination of polystyrene.[23] Their results indicate that destruction of aromaticity may be characteristic of F-atom reactions because it is most prevalent in plasmas (e.g., SF_6 and dilute F_2 plasmas) that are copious F-atom sources.[22]

CONCLUSIONS

Angle-dependent XPS has been used to obtain composition depth profiles of nonplanar surfaces. By incorporating the theoretical depth distribution function appropriate for cylindrical surfaces into the inversion program of Tyler et al., composition depth profiles of plasma-fluorinated PET fibers were obtained. The DDF for a hemispherical surface, which we propose can be used as a model for a randomly rough surface, was also derived; its application will be presented elsewhere.[20] Steps for improving the accuracy of the method are outlined. Composition depth profiles reveal that the F concentration decreases by ~ 50% within 10 Å of the surface, indicating that most fluorination occurs within the top few PET "monolayers." C1s difference spectra reveal that fluorination occurs preferentially on the phenyl ring, with formation of —CHF— and —CF_2— moieties. Observation of —CF_2— groups implies partial loss of aromaticity.

This paper is dedicated to the memory of Dr. Alan Buckley. We thank Jacqueline Ayotte for characterizing the angle-dependent sensitivity of the Kratos ES300 spectrometer. The help of Adrian Paris in preparing Figures 1, 2, 3, and 5 is gratefully acknowledged.

REFERENCES

1. Standard Definitions of Terms Relating to Surface Analysis (E673-82), *Surf. Interface Anal.*, **5**, 268 (1983); **10**, 48 (1987).
2. J. F. Moulder, W. F. Stickle, P. E. Sobol, and K. D. Bomben, *Handbook of X-ray Photoelectron Spectroscopy*, Perkin-Elmer Corp., Eden Prairie, MN, 1992, p. 25.
3. A. Jablonski and H. Ebel, *Surf. Interface Anal.*, **11**, 627 (1988).
4. M. H. Kalos and P. A. Whitlock, *Monte Carlo Methods, Vol. 1: Basics*, Wiley, New York, 1986, p. 18.
5. G. Gillberg and D. Kemp, *J. Appl. Polym. Sci.*, **26**, 2023 (1981).
6. B. J. Tyler, D. G. Castner, and B. D. Ratner, *Surf. Interface Anal.*, **14**, 443 (1989).
7. G. Gillberg, L. C. Sawyer, and A. L. Promislow, *J. Appl. Polym. Sci.*, **28**, 3723 (1983).
8. T. A. Dang, J. Cuddy, and S. Yang, *Surf. Interface Anal.*, **20**, 121 (1993).
9. F. Kaufman, *J. Phys. Chem.*, **88**, 4909 (1984).
10. J. A. McCaulley, PhD Dissertation, University of Pittsburgh, 1987.
11. W. E. Jones and E. G. Skolnik, *Chem. Rev.*, **76**, 563 (1976).
12. B. J. Tyler, D. G. Castner, and B. D. Ratner, *J. Vac. Sci. Technol. A*, **7**, 1646 (1989).
13. D. A. Shirley, *Phys. Rev. B*, **5**, 4709 (1972). Background subtraction and integration performed with ESCA TOOLS Version 2.1, Surface/Interface, Inc.
14. B. J. Tyler, private communication.
15. P. E. Laibnis, C. D. Bain, and G. M. Whitesides, *J. Phys. Chem.*, **95**, 7017 (1991).

16. M. P. Seah and W. A. Dench, *Surf. Interface Anal.*, **1,** 2 (1979).
17. V. B. Glasko, *Inverse Problems of Mathematical Physics,* AIP, New York, 1988.
18. G. C. Smith and A. K. Livesey, *Surf. Interface Anal.*, **19,** 175 (1992).
19. W. S. M. Werner and H. Stori, *Surf. Interface Anal.*, **19,** 83 (1992).
20. J. A. McCaulley and J. M. Ayotte, unpublished results.
21. G. N. Robinson, A. Freedman, and R. L. Graham, to appear.
22. M. Strobel, S. Corn, C. S. Lyons, and G. A. Korba, *J. Polym. Sci., Polym Chem.*, **25,** 1295 (1987).
23. M. Strobel, P. A. Thomas, and C. S. Lyons, *J. Polym. Sci., Polym. Chem.*, **25,** 3343 (1987).
24. R. Atkinson, *Kinetics and Mechanisms of the Gas-phase Reactions of the Hydroxyl Radical with Organic Compounds, J. Phys. Chem. Ref. Data,* Monograph 1 (1989).
25. D. Briggs, in *Practical Surface Analysis,* 2nd ed., *Vol. 1, Auger and X-ray Photoelectron Spectroscopy,* D. Briggs and M. P. Seah, Eds., Wiley, New York, 1990, p. 444.

Received August 30, 1993
Accepted January 24, 1994